INORGANIC CHEMISTRY FRONTIERS

RESEARCH ARTICLE

View Article Online
View Journal | View Issue

Cite this: *Inorg. Chem. Front.*, 2025, **12**, 6992

The role of anionic design in modulating material properties: from SHG switching to ferroelastic switching†

Jia-Zi She, Yun-Hui Yu, Yan-Ran Weng, Dan Lu, Yong Yu, Ying Zhou, Hui-Peng Lv and Yong Ai *

Received 6th June 2025,
Accepted 7th July 2025

DOI: 10.1039/d5qi01256b

rsc.li/frontiers-inorganic

Crystallographic engineering and chemical synthesis modification play crucial roles in modulating material properties and designing multifunctional materials, such as those with second-harmonic generation (SHG) switching and ferroelastic behaviors. Herein, we present the role of anion-based design in crystalline materials through anion H/F substitution. Specifically, the material $[NMe_4][CH_3SO_3]$ exhibits a high phase transition temperature (T_c = 462 K) and excellent SHG switching performance. The introduction of polyfluorinated substitutions results in a new organic ferroelastic material, $[NMe_4][CF_3SO_3]$, which exhibits ferroelastic phase transition at 309 K. The transition from the non-centrosymmetric $[NMe_4][CH_3SO_3]$ to the centrosymmetric $[NMe_4][CF_3SO_3]$ leads to a shift in material properties, transitioning from SHG switching to ferroelastic switching. Our findings underscore the importance of anion-based design in the development of advanced multifunctional phase-transition materials.

Introduction

Phase transition materials undergo alterations in their physical properties with temperature variations, exhibiting multiple functional characteristics, such as switchable second-order nonlinear optical (NLO), dielectric, ferroelastic, ferroelectric, *etc*.[1–10] Especially in second-harmonic generation (SHG) switching and ferroelastic switching materials, phase transitions play a crucial role. SHG switching materials driven by symmetry-breaking structural phase transitions have garnered considerable attention due to their unique combination of tunable optical properties and robust switching performance.[11–14] The mechanism relies on reversible transitions between centrosymmetric and non-centrosymmetric states, where symmetry changes during phase transitions induce sharp modulation of SHG responses, enabling reproducible 'on–off' switching.[15,16] Notably, organic molecular phase transition materials exhibit superior chemical tunability and dynamically adjustable nonlinear optical properties during phase transitions, resulting in excellent SHG switching performance.[17–20] During phase transitions, the material's crystal structure undergoes significant changes, leading to symmetry breaking that can induce ferroelastic behavior.[21,22] However, designing ferroelastic phase transitions necessitates adherence to one of the 94 ferroelastic phase transition types outlined in Aizu's rule.[23]

The low phase transition temperatures have significantly hindered the application and development of phase transition materials. Crystallographic engineering, particularly through fluorine substitution, plays a pivotal role in enhancing phase transition temperatures and modulating material properties.[24] The pronounced electronegativity difference between hydrogen and fluorine atoms induces substantial variations in molecular polarizability within H/F-substituted systems, potentially leading to significant alterations in macroscopic physical properties.[25] For instance, monofluorination leads to significant T_c enhancement in those hybrid molecular materials, such as (fluoropyrrolidinium)$MnCl_3$,[26] $[(CH_3)_3PCH_2F][Cd(SCN)_3]$,[27] *N*,*N*-dimethyl-3-fluoropyrrolidinium $CdCl_3$,[28] $(4FHQ)_2RbEu(NO_3)_6$[29] and so on.[30–33]

Furthermore, multiple fluorine substitutions on the cations demonstrate remarkable efficacy in modifying the transition temperature, polarity, photochromism, and crystal structures, as evidenced by those hybrid compounds, such as $[4,4\text{-DFPD}]_2PbI_4$,[34] $[4,4\text{-DFHHA}]_2PbI_4$,[35] $[3,3\text{-Difluorocyclobutylammonium}]_2\ CuCl_4$,[36] $[DFCBA]_2CrCl_4$.[37] Besides, multiple fluorine substitutions can also induce the weaker intermolecular interactions within amantadine-pentafluorobenzoic acid and lead to a ferroelastic phase transition.[38] In addition to modulating material properties through H/F substitution in the cationic part of mole-

Ordered Matter Science Research Center, Nanchang University, 330031, P. R. China. E-mail: yong.ai@ncu.edu.cn

†Electronic supplementary information (ESI) available: Fig. S1–S10 and Tables S1–S3. CCDC 2449758 and 2449759. For ESI and crystallographic data in CIF or other electronic format see DOI: https://doi.org/10.1039/d5qi01256b

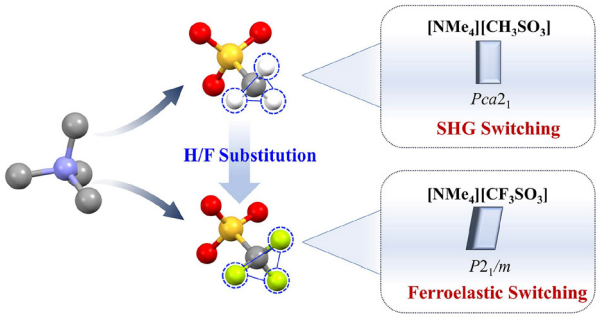

Scheme 1 The design strategy for SHG switching CH-NMe_4 and ferroelastic switching CF-NMe_4.

cular crystals, H/F substitution in the anionic component can also be used. Fu *et al.* reported the flexible organic ferroelectric material PEA-TFMS using an anionic fluorination strategy, showing the feasibility of inducing plastic ferroelectricity.[39] Sugata Ray achieved multiferroicity in fluorinated inorganic oxides, $Ca_2Mn_2O_{5-x}F_y$, by engineering anionic networks through fluorination and vacancy ordering.[24]

In this work, we explore the effects of H/F substitution on the anionic components to modulate the phase transition and crystalline symmetry. Herein, we choose quasi-spherical tetramethylammonium molecules as cation, which is prone to order–disorder phase transitions,[40–42] successfully constructed two multifunctional materials, namely $[NMe_4][CH_3SO_3]$ (CH-NMe_4) and $[NMe_4][CF_3SO_3]$ (CF-NMe_4). As shown in Scheme 1, the organic compound CH-NMe_4 exhibits high T_c of 462 K and SHG switching behaviours. CH-NMe_4 crystallizes in the non-centrosymmetric $Pca2_1$ space group at 293 K, demonstrating significant nonlinear optical switching with a large on–off ratio and high stability. In contrast, the H/F substituted compound CF-NMe_4 crystallizes in the centrosymmetric $P2_1/m$ space group at 260 K. Reversible ferroelastic domain patterns confirm its ferroelastic phase transition. This work highlights the synergy between crystallographic engineering and H/F substitution in tailoring material functionalities, offering valuable insights for advancing nonlinear optical materials and ferroelastics.

Results and discussion

Materials

Crystals of CH-NMe_4 and CF-NMe_4 are grown in ethanol solution, slowly evaporated by the solvent at a constant temperature of 30 °C, and colourless, clear crystals for single crystal measurement were obtained. Thermogravimetric analysis (TGA) confirms exceptional thermal stability, with decomposition onsets occurring at 634 K for CH-NMe_4 and 705 K for CF-NMe_4 (Fig. S1, ESI†), indicating their robust thermal stability.

Single crystal structures

At 293 K, the CH-NMe_4 crystallized in the orthorhombic $Pca2_1$ space group with cell parameter of a = 11.994(2) Å, b = 6.1359 (13) Å, c = 11.923(3) Å, $\alpha = \beta = \gamma = 90°$. The non-centrosymmetric crystalline structure of CH-NMe_4 demonstrated intrinsic piezoelectric behavior. Quasi-static measurements revealed a d_{33} coefficient of 11 pC N^{-1}, confirming its piezoelectric responsiveness (Fig. S2, ESI†). The CF-NMe_4 crystallized in the monoclinic $P2_1/m$ space group at 260 K. The parameters are a = 10.3722(3) Å, b = 8.6225(2) Å, c = 11.6086(3) Å, $\alpha = \gamma = 90°$, β = 103.824° for CF-NMe_4. The detailed cell parameters of CH-NMe_4 and CF-NMe_4 are listed in Table S1, ESI.† Subsequently, we performed powder X-ray diffraction (PXRD) to verify the phase purity. The experimental patterns show excellent agreement with simulated profiles (Fig. S3, ESI†), with all observed peaks aligning precisely with simulated reflections, confirming the phase purity of both CH-NMe_4 and CF-NMe_4. As depicted in Fig. 1a, the asymmetric unit of the CH-NMe_4 consists of one NMe_4^+ cation and one $CH_3SO_3^-$ anion. The $CH_3SO_3^-$ parameters for CH-NMe_4 are comparable to those found in the ordered phases of other known compounds with methanesulfonic acid,[43] with S–O bond lengths ranging from 1.446 to 1.458 Å. The $CH_3SO_3^-$ anion is involved in four non-classical hydrogen bonds C–H···O. The strongest hydrogen bonds in the structure exist between the O atom on the methanesulfonic acid and the N atom on the tetramethylamine, which are at the closest distance: H···A = 2.40 Å, D···A = 3.349 Å, D–H–A = 170° (Fig. 1b, Fig. S4a and Table S2, ESI†). Ions of opposite charges are alternately arranged along c-axis, forming a two-dimensional structure perpendicular to the b-axis under the weak interaction force. For CF-NMe_4, the asymmetric unit of the crystal structure consists of two NMe_4^+ cations and two $CH_3SO_3^-$ anions, as depicted in Fig. 1c. There exists C–H···O hydrogen-bonding interactions in the structure, forming infinite linear hydrogen-bonded chains along the b-axis, as shown in Fig. 1d and Fig. S4b, ESI.† The non-classical hydrogen bonds of the CH-NMe_4 and CF-NMe_4 crystals are summarized in Tables S2 and S3, ESI.† At 260 K, CF-NMe_4 exhibits six types of C–H···O hydrogen bonds, with bond lengths ranging from 3.373 Å to 3.442 Å, and corresponding bond angles ranging from 148° to 153°. Unlike most studies in which the introduction of monofluoro substitution brings

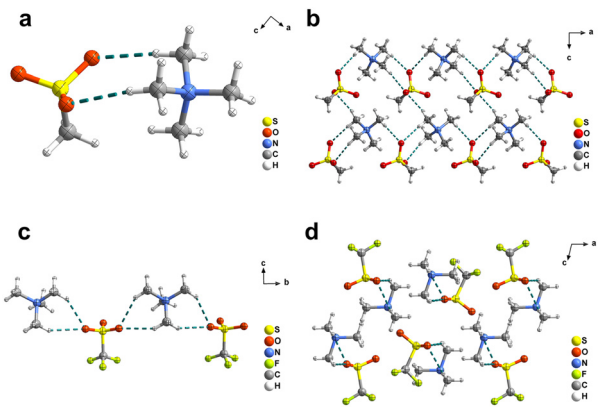

Fig. 1 The asymmetric unit of (a) CH-NMe_4 at 293 K and (c) CF-NMe_4 at 260 K. Packing structure of (b) CH-NMe_4 at 293 K and (d) CF-NMe_4 at 260 K. The dash lines denote the C–H···O hydrogen bond.

about polarity,[26,28,33] the multiple fluorine substitution on the anions induces a notable reduction in crystal symmetry, leading to the formation of a centrosymmetric structure in CF-NMe_4.

Hirshfeld surfaces analysis

The 2D fingerprint plots enable detailed analysis and highlight the interaction forces between specific atoms, allowing for separation based on the varying contribution levels of different interactions depicted in the Fig. 2. To further explore the influence of anion fluorination on molecular dynamics, Hirshfeld surfaces and 2D fingerprint plots (Fig. 2) were generated using CrystalExplorer software, leveraging their CIF files for detailed analysis. In Fig. 2a, six distinct red spots on the Hirshfeld surface of CH-NMe_4 signify the presence of C–H···O hydrogen bonds. A comprehensive analysis of the full 2D fingerprint plot in Fig. S5, ESI† further elucidates the relative contributions of various hydrogen bond types. Detailed analysis of the fingerprint plot reveals that H···H interactions dominate, contributing 65.2% of the total Hirshfeld surface area, while H···O interactions account for 34.7%. Additionally, the H···S.

Interaction represents only 0.1% of the Hirshfeld surface. In Fig. 2b, the Hirshfeld surface of CF-NMe_4 exhibits five prominent red spots, signifying the presence of C–H···O hydrogen bond interactions. Analyzing the fingerprint plot reveals that O···H interactions occupy 49.0% of the entire Hirshfeld surface area, while F···H interactions account for 42.4%. Further examination of the complete 2D fingerprint plot in Fig. S6, ESI† provides additional details about the contributions of various hydrogen bond types. Specifically, Fig. S6e, ESI† represents the F···F interaction, contributing 6.9% to the Hirshfeld surface, while Fig. S6f and S6g, ESI† depict the F···O/S···H interactions, accounting for 1.3% and 0.3%, respectively. Anionic fluorination markedly influences the spacing between H atoms on cations and O atoms on anions, thereby reshaping structural packing by introducing steric effects. Simultaneously, it reorganizes hydrogen-bonding network formation pathways through enhanced electrostatic interactions, highlighting the profound impact of fluorination on molecular arrangements.

Phase transitions

Differential Scanning Calorimetry (DSC) serves as a robust analytical tool for precisely identifying phase transitions triggered by external thermal stimuli. Then, DSC measurements were conducted to explore the phase transition behaviors of CH-NMe_4 and CF-NMe_4. During the heating and cooling cycle of CH-NMe_4, which ranged from 425 K to 490 K, a pair of endothermic and exothermic peaks were observed at 462 K and 453 K, respectively, as depicted in Fig. 3a. This observation indicates a reversible phase transition. Notably, the significant temperature hysteresis effect during the heating and cooling processes is characteristic of first-order phase transitions.[44] It is noteworthy that CH-NMe_4 exhibits an exceptionally high phase transition temperature (462 K), which significantly exceeds that most of organic materials,[45–54] underscoring its unique thermal stability. For CF-NMe_4, within the temperature range of 250–330 K, during the heating/cooling cycle, the DSC curve exhibits a pair of distinct thermal anomaly peaks at 309 K/283 K (Fig. 3b). The corresponding entropy changes (ΔS) for the endothermic peaks are approximately 2.98 and 17.9 J mol^{-1} K^{-1} for CH-NMe_4 and CF-NMe_4, respectively. Upon fluorination of the methanesulfonic acid anions, the phase transition temperature changes from 462 K to 309 K.

Phase transitions are typically accompanied by dielectric anomalies. Temperature-dependent dielectric measurements were performed at 1 MHz during a heating–cooling thermal cycle. For CH-NMe_4, a step-like dielectric anomaly is observed near 460 K (Fig. 3c), marked by a discontinuous increase in the real permittivity (ε') from 10.8 (low dielectric state) to 22.7 (high dielectric state), representing a 2.1-fold enhancement. Similarly, CF-NMe_4 demonstrates distinct dielectric behavior: during heating, ε' gradually increases from 4.5 at 307 K to 7.8

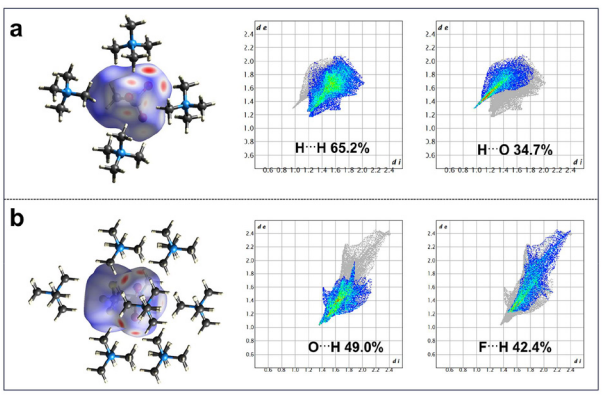

Fig. 2 Visualization map of the distribution of the interactions and the two-dimensional fingerprint plots of (a) CH-NMe_4, and (b) CF-NMe_4, show contributions from $H_{outside}$–O_{inside}.

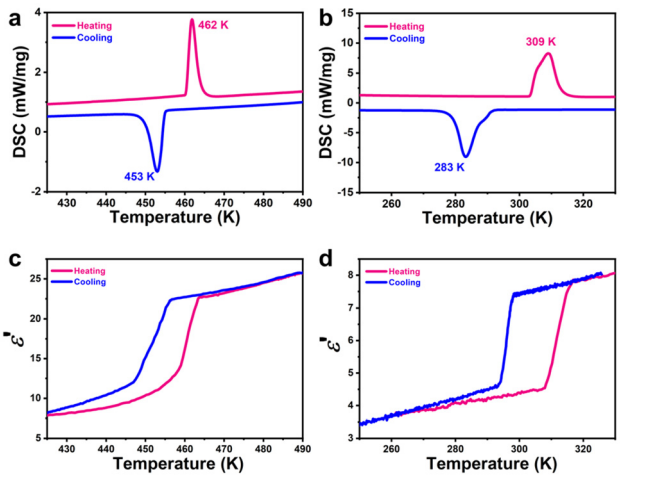

Fig. 3 The DSC curves for (a) CH-NMe_4 and (b) CF-NMe_4. The temperature-dependent real part (ε') of the dielectric constant was measured at 1 MHz for (c) CH-NMe_4 and (d) CF-NMe_4.

at 317 K, followed by stabilization ($\Delta\varepsilon' < 0.5$) at elevated temperatures (Fig. 3d). The value of ε' in the high dielectric state is about 1.73 times that in the low dielectric state. The permittivity-temperature profiles were also measured at 1, 5, 10, and 100 kHz (Fig. S7, ESI†). As shown in Fig. S7,† the dielectric constant decreased with increasing frequency. Furthermore, the T_c deduced from permittivity-temperature curves is frequency-independent. Both compounds display thermal hysteresis (>5 K) between heating/cooling cycles, consistent with first-order transition characteristics observed in DSC.

To elucidate the structural phase transition, we attempted to measure the high-temperature crystal structures of CH-NMe_4 and CF-NMe_4. However, weak diffraction and severe ionic disorder at elevated temperatures hindered the successful collection of high-temperature phase data. Variable-temperature PXRD measurements were conducted for further analysis. A marked change in peak positions and intensities was observed upon heating to the phase transition point (Fig. S8, ESI†), confirming the occurrence of phase transition behavior leading to symmetry breaking. Critical evidence emerges from the progressive simplification of diffraction patterns, where specific reflections vanish above the transition temperature alongside reduced peak multiplicity. Rietveld refinement of high-temperature PXRD data reveals distinct structural transformations: CH-NMe_4 transitions from an orthorhombic *mm*2 system to a tetragonal system, while CF-NMe_4 undergoes monoclinic 2/*m* to tetragonal symmetry elevation (Fig. S9 and S10, ESI†). Although CH-NMe_4 exhibits a polar crystal structure that satisfies the symmetry requirements for ferroelectricity, the piezoresponse force microscopy analysis showed no evidence of domain switching or polarization hysteresis under various experimental conditions.

SHG switching

The temperature-dependent second-harmonic generation (SHG) serves as a sensitive probe for identifying structural transformations between centrosymmetric and non-centrosymmetric states.[16,55] To further investigate the symmetry changes associated with the phase transition, we conducted SHG measurements on CH-NMe_4. At room temperature, CH-NMe_4 demonstrates a moderate SHG intensity, measuring 0.8 times that of KDP (Fig. 4a), which aligns with its non-centrosymmetric packing in the $Pca2_1$ space group. Temperature-dependent SHG measurements demonstrate a distinct bistable response, as illustrated in Fig. 4b. During heating, strong SHG signals persist below 460 K (high-NLO state) but abruptly vanish above 480 K as the material transitions to a centrosymmetric phase (low-NLOstate). Conversely, upon cooling, the SHG response of CH-NMe_4 remains zero until 477 K before sharply recovering at 466 K with a 5.6 V signal, demonstrating a 9 K thermal hysteresis. The complete suppression of SHG intensity in the high-temperature phase confirms symmetry elevation to a centrosymmetric space group. Remarkably, CH-NMe_4 retains over 95% of its initial SHG intensity across 10 thermal cycles (Fig. 4c), achieving an exceptional switching contrast ratio ($I_{on}/I_{off} \approx 13$) that outperforms many existing SHG-switching materials.[55–58] This unique combination of robust bistability, high switching contrast, and exceptional durability establishes CH-NMe_4 as a highly promising candidate for nonlinear optical switching devices that demand precise state control and long-term operational stability.[59] In contrast, the fluorine-substituted analogue, CF-NMe_4, crystallizes in a centrosymmetric space group and thus shows no SHG signal.

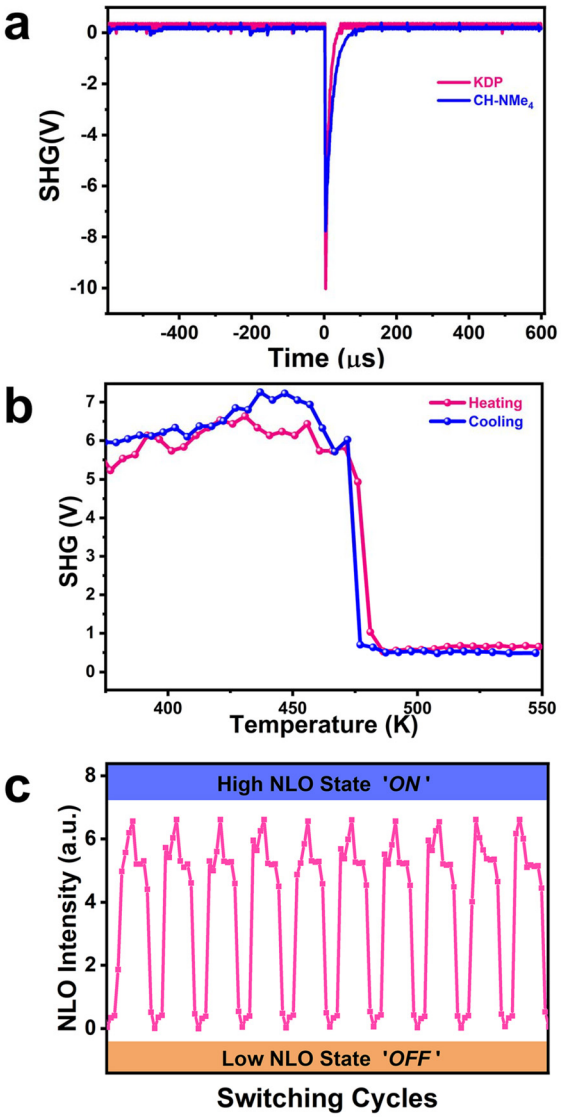

Fig. 4 (a) SHG signals of CH-NMe_4 and KDP at room temperature. (b) The temperature dependencies of SHG signals under heating and cooling run of CH-NMe_4. (c) Cycles of switching high and low NLO states of SHG signals of CH-NMe_4.

Ferroelastic switching

The evolution of ferroelastic domains is a sign of ferroelastic phase transitions, which we investigated through temperature-dependent polarized light microscopy. For CF-NMe_4, the appearance of stripe-like patterns in polarized microscopy

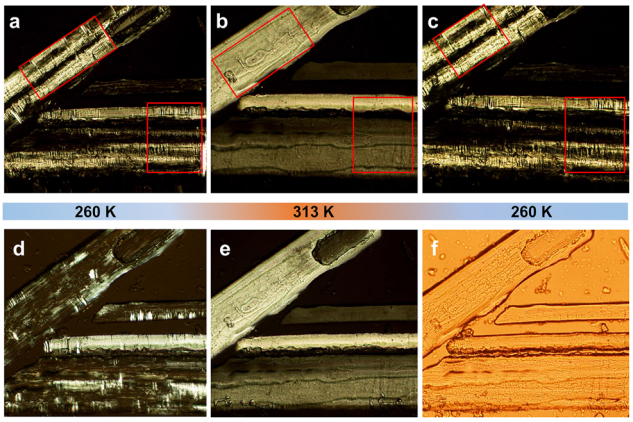

Fig. 5 The ferroelastic domain walls evolution of CF-NMe_4. (a–e) evolutions of the ferroelastic domain structure for CF-NMe_4 in the cooling-heating runs, natural optical microscope images for (f) morphology of CF-NMe_4. Ferroelastic domain evolution is indicated by the red rectangular frame.

images (at 260 K, Fig. 5a) serves as a definitive indicator of ferroelastic domain formation, which is distinct from material morphology (Fig. 5f). These domains exhibit alternating light–dark contrast, originating from the coexistence of multiple spontaneous strain orientations during the paraelastic-to-ferroelastic transition. Upon gradual heating, the ferroelastic domain structure progressively diminishes and fully vanishes near 313 K (Fig. 5b and e), signaling the transition to a paraelastic phase. The domain patterns reversibly reappear with restored stripe-like domain walls upon cooling back to 260 K (Fig. 5c and d), demonstrating robust thermal cyclability and highlighting the material's structural reversibility. DSC and temperature-dependent PXRD analyses confirm a reversible phase transition near 309 K. The temperature-dependent domain switching dynamics, coupled with the hysteretic recovery of domain patterns, provide unequivocal evidence of ferroelasticity in CF-NMe_4. However, no significant ferroelastic domain evolution was observed in CH-NMe_4, leading us to conclude that it lacks ferroelasticity. This structural transformation profoundly influences the material's properties, highlighting the critical role of chemical modifications in tailoring functional behaviors.

Conclusions

In conclusion, we reported an organic nonlinear optical switching material CH-NMe_4, and a molecular ferroelastic CF-NMe_4. Structural analyses reveal that the polyfluorinated substitution on the anion markedly alters intermolecular interactions and packing arrangements, inducing a transformation from a non-centrosymmetric (space group $Pca2_1$) to a centrosymmetric (space group $P2_1/m$) crystal structure at room temperature. Through anion modification, both symmetry breaking and lattice flexibility are simultaneously regulated, resulting in the disappearance of polarity and triggering ferroelasticity. This work realizes the functional switching of phase transition materials through anion fluorination, demonstrating an effective chemical synthesis strategy and providing ideas for the development of multifunctional materials.

Conflicts of interest

There are no conflicts to declare.

Data availability

The data supporting this article have been included as part of the ESI.† Crystallographic data has been deposited at the Cambridge Crystallographic Data Centre (CCDC) as a supplementary publication no. 2449758 and 2449759.

Acknowledgements

This work was supported by the National Natural Science Foundation of China (No. 22271131 and 22401132).

References

1 Z.-X. Zhang, T. Zhang, P.-P. Shi, W.-Y. Zhang, Q. Ye and D.-W. Fu, Exploring high-performance integration in a plastic crystal/film with switching and semiconducting behavior, *Inorg. Chem. Front.*, 2020, **7**, 1239–1249.
2 H. Zhang, L. Wang, W. Guo, H. Cai and Z. Wei, An organic–inorganic hybrid material $[Me_3NCH_2CH_2F]FeBr_4$ exhibits three-step SHG on/off, *Chem. Commun.*, 2023, **59**, 13442–13445.
3 Y. He, Z. Chen, X. Chen, X.-M. Zhang and D. Fu, High temperature hybrid perovskite multifunctional switching materials constructed through precise molecular design, *Mater. Chem. Front.*, 2022, **6**, 1292–1300.
4 P. Liu, Y. Gao and X. Chen, Magnetically tightened multifunctional phase change materials, *Matter*, 2022, **5**, 1639–1642.
5 H.-Q. Yao, Z. Ding, S.-Y. Zhang, Y.-F. Wu, X. Qiu, Y. Peng, H.-Y. Ye and Z.-B. Hu, High temperature synergistic response of magnetism, dielectricity, and luminescence in a Mn(ii)-based molecular organic–inorganic hybrid, *CrystEngComm*, 2024, **26**, 1767–1772.
6 K. Li, Z.-G. Li, J. Xu, Y. Qin, W. Li, A. Stroppa, K. T. Butler, C. J. Howard, M. T. Dove, A. K. Cheetham and X.-H. Bu, Origin of Ferroelectricity in Two Prototypical Hybrid Organic–Inorganic Perovskites, *J. Am. Chem. Soc.*, 2022, **144**, 816–823.
7 T.-M. Guo, F.-F. Gao, Y.-J. Gong, Z.-G. Li, F. Wei, W. Li and X.-H. Bu, Chiral Two-Dimensional Hybrid Organic–Inorganic Perovskites for Piezoelectric Ultrasound Detection, *J. Am. Chem. Soc.*, 2023, **145**, 22475–22482.

8 L.-A. Gui, Y.-F. Zhang, Y. Peng, Z.-B. Hu and Y. Song, Synergetic Responses of Multiple Functions Induced by Phase Transition in Molecular Materials, *ChemPhysChem*, 2024, **25**, e202400297.
9 C. Shi, X.-B. Han and W. Zhang, Structural phase transition-associated dielectric transition and ferroelectricity in coordination compounds, *Coord. Chem. Rev.*, 2019, **378**, 561–576.
10 C. Yang, J. Gou, Y. Zhu, Y. Xiong, Z. Zhu, L. Chen and Q. Wu, Unconventional Heterobidentate Coordination of 4-Hydroxypyridine Leading to Remarkably Strong Second-Harmonic Generation in $Zn(C_5H_4NO)_2$, *Angew. Chem., Int. Ed.*, 2025, **64**, e202420810.
11 Y. Wang, T. Zhang, M.-M. Lun, F.-L. Zhou, D.-W. Fu and Y. Zhang, Halogen regulation triggers NLO and dielectric dual switches in hybrid compounds with green fluorescence, *Inorg. Chem. Front.*, 2021, **8**, 4230–4238.
12 C.-Y. Pan, X.-R. Yang, L. Xiong, Z.-W. Lu, B.-Y. Zhen, X. Sui, X.-B. Deng, L. Chen and L.-M. Wu, Solid-State Nonlinear Optical Switch with the Widest Switching Temperature Range Owing to Its Continuously Tunable T_c, *J. Am. Chem. Soc.*, 2020, **142**, 6423–6431.
13 X.-N. Hua, W.-Y. Zhang and P.-P. Shi, Two-step nonlinear optical switch in a hydrogen-bonded perovskite-type crystal, *Chem. Commun.*, 2022, **58**, 1712–1715.
14 Z.-B. Hu, X. Yang, J. Zhang, L.-A. Gui, Y.-F. Zhang, X.-D. Liu, Z.-H. Zhou, Y. Jiang, Y. Zhang, S. Dong and Y. Song, Molecular ferroelectric with low-magnetic-field magnetoelectricity at room temperature, *Nat. Commun.*, 2024, **15**, 4702.
15 M. Yang, H. Cheng, Y. Xu, M. Li and Y. Ai, A hybrid organic-inorganic perovskite with robust SHG switching, *Chin. Chem. Lett.*, 2022, **33**, 2143–2146.
16 L. He, P.-P. Shi, M.-M. Zhao, C.-M. Liu, W. Zhang and Q. Ye, Emergent Chirality and Nonlinear Optical Switching in a Ferroelastic Molecular Perovskite Solid Solution, *Chem. Mater.*, 2021, **33**, 799–805.
17 T. Tian, Y. Fang, W. Wang, M. Yang, Y. Tan, C. Xu, S. Zhang, Y. Chen, M. Xu, B. Cai and W.-Q. Wu, Durable organic nonlinear optical membranes for thermotolerant lightings and in vivo bioimaging, *Nat. Commun.*, 2023, **14**, 4429.
18 R. Agilandeshwari, V. Meenatchi and S. P. Meenakshisundaram, Synthesis, growth, structure and characterization of chalcone crystal: A novel organic NLO material, *J. Mol. Struct.*, 2016, **1118**, 356–366.
19 H. Zhang, Y. Tian, S. Bo, L. Xiao, Y. Ao, J. Zhang and M. Li, A study on regulating the conjugate position of NLO chromophores for reducing the dipole moment and enhancing the electro-optic activities of organic materials, *J. Mater. Chem. C*, 2019, **8**, 1380–1390.
20 B. B. Ivanova and M. Spiteller, Possible Application of the Organic Barbiturates as NLO Materials, *Cryst. Growth Des.*, 2010, **10**, 2470–2474.
21 V. K. Wadhawan, Ferroelasticity, *Bull. Mater. Sci.*, 1984, **6**, 733–753.
22 Y. Zeng, J. Liu, L. Zhou, X. Deng, W. Yang, X. Yan, Y. Luo, X. Zhu, X. Huang, X. Song and Y. Tang, An organic-inorganic hybrid thermochromic ferroelastic with multi-channel switches, *Chin. Chem. Lett.*, 2023, **34**, 108127.
23 K. Aizu, Determination of the State Parameters and Formulation of Spontaneous Strain for Ferroelastics, *J. Phys. Soc. Jpn.*, 1970, **28**, 706–716.
24 P. Aich, S. Das, S. Halder, C. Meneghini, D. Fu, V. Siruguri, S. D. Kaushik, M. Itoh, T. Saha-Dasgupta and S. Ray, Fluorination-Induced Asymmetry in Vacancy-Ordered Brownmillerite: Route to Multiferroic Behavior, *Chem. Mater.*, 2023, **35**, 991–998.
25 H.-P. Lv, Y.-R. Li, X.-J. Song, N. Zhang, R.-G. Xiong and H.-Y. Zhang, A Poling-Free Supramolecular Crown Ether Compound with Large Piezoelectricity, *J. Am. Chem. Soc.*, 2023, **145**, 3187–3195.
26 Y. Ai, X.-G. Chen, P.-P. Shi, Y.-Y. Tang, P.-F. Li, W.-Q. Liao and R.-G. Xiong, Fluorine Substitution Induced High T_c of Enantiomeric Perovskite Ferroelectrics: (*R*)- and (*S*)-3-(Fluoropyrrolidinium)$MnCl_3$, *J. Am. Chem. Soc.*, 2019, **141**, 4474–4479.
27 Y.-J. Cao, L. Zhou, P.-P. Shi, Q. Ye and D.-W. Fu, H/F substituted perovskite compounds with above-room-temperature ferroelasticity: $[(CH_3)_4P][Cd(SCN)_3]$ and $[(CH_3)_3PCH_2F][Cd(SCN)_3]$, *Chem. Commun.*, 2019, **55**, 8418–8421.
28 H. Peng, H. Cheng, Y.-H. Liu, M.-J. Yang, W.-Q. Liao and Y. Ai, Enantiomeric perovskite with a dual phase transition at high temperature, *J. Mater. Chem. C*, 2021, **9**, 1918–1922.
29 Q. Xu, L. Ye, R.-M. Liao, Z. An, C.-F. Wang, L.-P. Miao, C. Shi, H.-Y. Ye and Y. Zhang, Front Cover: H/F Substitution Induced Large Increase of T_c in a 3D Hybrid Rare-Earth Double Perovskite Multifunctional Compound (Chem. Eur. J. 14/2022), *Chem. – Eur. J.*, 2022, **28**, e202200520.
30 Z. Hendi, S. Jamali, S. Mahmoudi, H. Samouei, S. Nayeri, S. M. J. Chabok and Z. Jamshidi, Metal–Organic Cubane Cage with Trimethylplatinum(IV) Vertices, *Inorg. Chem.*, 2022, **61**, 15–19.
31 N. Zhang, W. Sun, Y. Zhang, H.-H. Jiang, R.-G. Xiong, S. Dong and H.-Y. Zhang, Organic radical ferroelectric crystals with martensitic phase transition, *Nat. Commun.*, 2023, **14**, 5854.
32 Y. Ai, R. Sun, Y.-L. Zeng, J.-C. Liu, Y.-Y. Tang, B.-W. Wang, Z.-M. Wang, S. Gao and R.-G. Xiong, Coexistence of magnetic and electric orderings in a divalent Cr^{2+}-based multiaxial molecular ferroelectric, *Chem. Sci.*, 2021, **12**, 9742–9747.
33 Y. Ai, D.-J. Wu, M.-J. Yang, P. Wang, W.-H. He and W.-Q. Liao, Highest-Tc organic enantiomeric ferroelectrics obtained by F/H substitution, *Chem. Commun.*, 2020, **56**, 7033–7036.
34 C.-R. Huang, X. Luo, X.-G. Chen, X.-J. Song, Z.-X. Zhang and R.-G. Xiong, A multiaxial lead-free two-dimensional organic-inorganic perovskite ferroelectric, *Natl. Sci. Rev.*, 2020, **8**, nwaa232.
35 H.-Y. Zhang, X.-J. Song, X.-G. Chen, Z.-X. Zhang, Y.-M. You, Y.-Y. Tang and R.-G. Xiong, Observation of Vortex Domains

in a Two-Dimensional Lead Iodide Perovskite Ferroelectric, *J. Am. Chem. Soc.*, 2020, **142**, 4925–4931.

36 X.-G. Chen, X.-J. Song, Z.-X. Zhang, H.-Y. Zhang, Q. Pan, J. Yao, Y.-M. You and R.-G. Xiong, Confinement-Driven Ferroelectricity in a Two-Dimensional Hybrid Lead Iodide Perovskite, *J. Am. Chem. Soc.*, 2020, **142**, 10212–10218.

37 Y. Ai, R. Sun, W.-Q. Liao, X.-J. Song, Y.-Y. Tang, B.-W. Wang, Z.-M. Wang, S. Gao and R.-G. Xiong, Unprecedented Ferroelectricity and Ferromagnetism in a Cr^{2+}-Based Two-Dimensional Hybrid Perovskite, *Angew. Chem., Int. Ed.*, 2022, **61**, e202206034.

38 L.-X. Zhou, W.-X. Mao, J.-F. Lan, X. Deng, Y. Qin and H.-Y. Zhang, Dual-Channel Control of Ferroelasticity in a Soft Molecular Crystal Induced by Perfluorinated Substitution, *Chem. Mater.*, 2024, **36**, 8976–8983.

39 P.-Z. Huang, Z. Liu, L.-K. Ye, H.-F. Ni, J.-Q. Luo, G. Teri, Q.-Q. Jia, B. Zhuang, C.-F. Wang, Z.-X. Zhang, Y. Zhang and D.-W. Fu, Mechanically deformable organic ferroelectric crystal with plasticity optimized by fluorination, *Nat. Commun.*, 2025, **16**, 3071.

40 A. Mertens, D. van Gerven, H. Lee and M. S. Wickleder, Synthesis and Characterization of the Trichlates $[N(CH_3)_4][Cl_3CSO_3]$, $[NH_4][Cl_3CSO_3]$, and the Dichlate $[NH_4][Cl_2CHSO_3]$, *Eur. J. Inorg. Chem.*, 2024, **27**, e202300535.

41 Y.-B. Li, X.-X. Chen, W.-J. Xu, Y.-P. Gong, H. Ye, Z.-S. Wang and W.-X. Zhang, Designing dynamic coordination bonds in polar hybrid crystals for a high-temperature ferroelastic transition, *Chem. Sci.*, 2024, **15**, 3661–3669.

42 M. L. Tarlton, T. D. Persinger, N. M. Byrne, T. C. Douglas, A. Yakovenko and R. E. Wilson, Rare Earth Nitrate Hybrid Double Perovskites $[Me_4N]_2[MLn(NO_3)_6]$ (M = Na–Cs; Ln = La–Gd, ex. Pm), *Inorg. Chem.*, 2023, **62**, 16770–16781.

43 M. Zegke, D. Grödler, M. R. Jungfer, A. Haseloer, M. Kreuter, J. M. Neudörfl, T. Sittel, C. M. James, J. Rothe, M. Altmaier, A. Klein, M. Breugst, U. Abram, E. Strub and M. S. Wickleder, Ammonium Pertechnetate in Mixtures of Trifluoromethanesulfonic Acid and Trifluoromethanesulfonic Anhydride, *Angew. Chem., Int. Ed.*, 2022, **61**, e202113777.

44 Y.-L. Zeng, X.-Q. Huang, C.-R. Huang, H. Zhang, F. Wang and Z.-X. Wang, Unprecedented 2D Homochiral Hybrid Lead-Iodide Perovskite Thermochromic Ferroelectrics with Ferroelastic Switching, *Angew. Chem., Int. Ed.*, 2021, **60**, 10730–10735.

45 K. Mencel, P. Durlak, M. Rok, R. Jakubas, J. Baran, W. Medycki, A. Ciżman and A. Piecha-Bisiorek, Widely used hardly known. An insight into electric and dynamic properties of formamidinium iodide, *RSC Adv.*, 2018, **8**, 26506–26516.

46 M. Węcławik, P. Szklarz, W. Medycki, R. Janicki, A. Piecha-Bisiorek, P. Zieliński and R. Jakubas, Unprecedented transformation of $[I^-{\cdot}I_3^-]$ to $[I_4^{2-}]$ polyiodides in the solid state: structures, phase transitions and characterization of dipyrazolium iodide triiodide, *Dalton Trans.*, 2015, **44**, 18447–18458.

47 T. J. Bednarchuk, V. Kinzhybalo, E. Markiewicz, B. Hilczer and A. Pietraszko, Structure, dielectric and electric properties of diisobutylammonium hydrogen sulfate crystal, *J. Solid State Chem.*, 2018, **258**, 753–761.

48 A. Piecha-Bisiorek, A. Białońska, R. Jakubas, P. Zieliński, M. Wojciechowska and M. Gałązka, Strong Improper Ferroelasticity and Weak Canted Ferroelectricity in a Martensitic-Like Phase Transition of Diisobutylammonium Bromide, *Adv. Mater.*, 2015, **27**, 5023–5027.

49 J. Meng, Y. Su, H. Zhu and T. Cai, Shape memory and self-healing in a molecular crystal with inverse temperature symmetry breaking, *Chem. Sci.*, 2024, **15**, 5738–5745.

50 H. Xu, W. Guo, Y. Ma, Y. Liu, X. Hu, L. Hua, S. Han, X. Liu, J. Luo and Z. Sun, Record high-T_c and large practical utilization level of electric polarization in metal-free molecular antiferroelectric solid solutions, *Nat. Commun.*, 2022, **13**, 5329.

51 Z. Chen, M. Li, J. Lan, S. Hu and X. Chen, Organic ferroelastic enantiomers with high Tc and large dielectric switching ratio triggered by order-disorder and displacive phase transition, *Chin. Chem. Lett.*, 2024, **35**, 109548.

52 D.-W. Fu, J.-X. Gao, P.-Z. Huang, R.-Y. Ren, T. Shao, L.-J. Han, J. Liu and J.-M. Gong, Observation of Transition from Ferroelasticity to Ferroelectricity by Solvent Selective Effect in Anilinium Bromide, *Angew. Chem., Int. Ed.*, 2021, **60**, 8198–8202.

53 J. Li, T. Zhang, M.-M. Lun, C.-Y. Su, Z.-X. Zhang, P.-Z. Huang, Y. Zhang, G. Teri and D.-W. Fu, Nicotinic acid bromide: a simple organic salt optical-electrical ferroelastic with high T_c, *Chem. Commun.*, 2023, **59**, 4644–4647.

54 Y. Zhang, K. Awaga, H. Yoshikawa and R.-G. Xiong, Ferroelastic phase transition and dielectric anomalies in 2,4,6-trimethylanilinium perchlorate, *J. Mater. Chem.*, 2012, **22**, 9841–9845.

55 T. Zhang, J.-Y. Li, G.-W. Du, K. Ding, X.-G. Chen, Y. Zhang and D.-W. Fu, Thermally-driven unusual dual SHG switching with wide SHG-active steps triggered by inverse symmetry breaking, *Inorg. Chem. Front.*, 2022, **9**, 4341–4349.

56 X. Lin, Y. Lv, X. Li, Z. Yue, K. Li, Q. Wei, Q. Wang, J. Luo and X. Liu, Rational design of a high-efficiency lead halide organic-inorganic hybrid nonlinear optical switch via molecular engineering, *Chin. Chem. Lett.*, 2025, 111083.

57 M.-Y. Guo, M.-F. Li, X.-X. Chen, W.-J. Xu and W.-X. Zhang, Equatorial–Axial Conformational Dynamics Enabling Thermoresponsive SHG Switch in a Homochiral Hybrid Compound, *ACS Appl. Opt. Mater.*, 2024, **2**, 2612–2620.

58 C. Shi, L. Ye, Z.-X. Gong, J.-J. Ma, Q.-W. Wang, J.-Y. Jiang, M.-M. Hua, C.-F. Wang, H. Yu, Y. Zhang and H.-Y. Ye, Two-Dimensional Organic–Inorganic Hybrid Rare-Earth Double Perovskite Ferroelectrics, *J. Am. Chem. Soc.*, 2020, **142**, 545–551.

59 Z. Yan, J. Fan, S. Pan and M. Zhang, Recent advances in rational structure design for nonlinear optical crystals: leveraging advantageous templates, *Chem. Soc. Rev.*, 2024, **53**, 6568–6599.

